



Applicability of two hybrid sound prediction methods for assessing in-duct sound absorbers of turbocharger compressors

Clemens Freidhager^{1,*}, Stefan Schoder¹, Paul Maurerlehner¹, Andreas Renz², Stefan Becker², and Manfred Kaltenbacher¹

¹Graz University of Technology, IGTE, Inffeldgasse 18, 8010 Graz, Austria

²Friedrich-Alexander Universität Erlangen-Nürnberg, Cauerstraße 4, 91058 Erlangen, Germany

Received 14 March 2022, Accepted 24 June 2022

Abstract – We analyze the differences between the Ffowcs–Williams and Hawking’s approach and a new sound propagation approach based on the finite element method used for solving Lighthill’s aeroacoustic wave equation for compressible flows. In addition, we discuss the applicability of both methods. The sound propagation approach based on Lighthill’s equation introduces a flow-interface boundary condition, similar to permeable boundaries in the Ffowcs–Williams and Hawking’s analogy, which allows the omission of complex geometries in propagation domains. This enables to reduce numeric effort and storage requirements. Thereby, the hybrid aeroacoustic workflow is considered, for which aeroacoustic source terms are computed to couple a flow and a separated acoustic propagation simulation. We present an extensive investigation of Lighthill’s source terms in the sense of the proposed weak formulation of Lighthill’s equation. For validation, measurements from a cold gas test rig are used. In addition, the possibilities of applying both sound propagation methods for investigating the influence of resonators and sound absorbers are discussed.

Keywords: Aeroacoustic, Lighthill, Ffowcs Williams-Hawkings

1 Introduction

One of the primary sources of noise pollution are technical devices [1]. The noise produced by technical applications is mainly connected to transportation, most often airplanes and highway vehicles [2]. As a result, in 2014, the European Commission introduced the regulation (EU) 540/2014 [3] for reducing noise in the automotive industry by 25% until the last implementation phase starting in 2024. As reference noise of the automotive industry, the year 2014 was considered. This is in agreement with the 17 sustainable development goals established by the United Nations [4]. Consequently, noise from car power units has recently become of great interest for industry-related science.

A common approach for investigating aeroacoustic phenomena is using simulations. However, because of the disparity of scales, current computational limitations do not allow direct simulations of flow and acoustics in complex technical applications [5, 6]. As a result, a general approach in literature is performing flow simulations using a compressible Detached Eddy Simulation (DES), in most cases with an underlying $k-\omega$ shear stress transport (SST) turbulence model [7–14], or a compressible Large Eddy Simulation (LES) [15–19]. Performing compressible flow simulations

has two major disadvantages. Firstly, flow simulation solvers are affected by numeric dissipation [17, 20], which becomes problematic for investigating acoustic propagation. The phenomenon of numerical dissipation is particularly problematic for low-order solvers and can be mitigated by finer discretization [20]. However, this significantly increases the numerical effort. Secondly, performing flow simulations of complex applications is computationally expensive. Depending on the available computational resources, computing enhanced flow simulations takes a lot of time, making it impractical to design and assess resonators and sound absorbers, which are common to reduce noise in ducted systems. This paper will discuss two different approaches to overcome these limitations. Firstly, by applying the integral Ffowcs Williams and Hawking’s (FW–H) analogy [17, 21], restrictions due to numeric dissipation do not affect simulation results. However, for in-duct simulations using the FW–H analogy, the limitations arising from the used free-field Green’s function have to be taken into account. The second approach for coping with the restrictions of flow solvers is a novel Lighthill propagation approach (LH-FE) for compressible flows based on the Finite Element (FE) method. LH-FE allows quickly incorporating different resonator and sound absorbers geometries [22]. Various works have already dealt with LH-FE in incompressible flows [23–25]. Furthermore, in 2005, Caro et al. [26] applied

*Corresponding author: clemens.freidhager@gmx.at

Lighthill's equation in combination with the FE method to an incompressible flow, to a pseudo compressible flow, where minor density variations are accounted for in the continuity equation, and to an isentropic flow, where the density is only a function of the pressure. However, none of those three cases account for the highly compressible flow with local Mach numbers $Ma > 1$ as in a turbocharger compressor. Consequently, we present an LH-FE approach coping with compressible flows. In addition, we investigate both the LH-FE approach and the FW-H approach by applying them to a turbocharger compressor. Furthermore, for validation of simulation results, cold gas test rig measurements were used. Finally, the applicability of the LH-FE approach for optimizing duct systems acoustically is shown by investigating the influence of a resonator insert.

This research article is structured as follows: Section 2 provides explanations of the considered FW-H approach (see Sect. 2.1) and the LH-FE approach (see Sect. 2.2). In Section 3, the flow and propagation setups are discussed. In Section 4, an extensive investigation of Lighthill's source terms is performed. In addition, flow and propagation simulations simulation results are investigated and validated with measurements. Furthermore, in Section 4.3, general applicability and practical aspects of the LH-FE approach are discussed. Finally, the presented work is concluded in Section 5.

2 Methodology

Subsequently, the FW-H analogy and the LH-FE are discussed. Both sound propagation approaches are based on compressible flow simulations, which have to be performed beforehand. Furthermore, both approaches rest on Lighthill's inhomogeneous wave equation [27, 28] which reads as

$$\left(\frac{1}{c_0^2} \frac{\partial^2}{\partial t^2} - \Delta\right)(c_0^2 \rho') = \nabla \cdot \nabla \cdot [\mathbf{L}]. \quad (1)$$

Thereby, c_0 denotes the ambient speed of sound, Δ the Laplace operator, $\rho' = \rho - \rho_0$ the density fluctuations, and ∇ the Nabla operator. Lighthill's equation directly reformulates the compressible flow equations without any simplifications. Lighthill's stress tensor $[\mathbf{L}]$ can be separated into three main parts, (1) a part due to Reynolds stresses, (2) an excess part, and (3) a part due to viscous stresses

$$[\mathbf{L}] = \underbrace{\rho \mathbf{v} \otimes \mathbf{v}}_{\text{Reynolds stress term}} + \underbrace{(p' - c_0^2 \rho')}_{\text{Excess term}} [\mathbf{I}] - \underbrace{[\boldsymbol{\tau}]}_{\text{Viscous term}}. \quad (2)$$

For low Mach number flows, the principal sound generators are the fluctuating Reynolds stresses. Consequently for $Ma < 0.3$ the *Reynolds stress term* becomes dominant [27, 29]. Furthermore, the *excess term* describes density deviation in the source flow with respect to the mean flow. As a result, the *excess term* becomes dominant for high Mach number "Ma" flows, as well as for thermoacoustics [29, 30] and combustion noise [31]. The *viscous stress* term, however, is only contributing substantially for small

Reynolds numbers "Re" [32]. Consequently, the *viscous stress* term is neglected for most technical applications, as shown in Section 4.1.

2.1 Ffowcs-Williams and Hawking's Analogy

Currently, the FW-H's analogy [21] is presumably one of the most used analogies for computing far-field pressure propagation of moving geometries [17, 33]. Considering $[\mathbf{P}] = (p - p_0)[\mathbf{I}]$ as the differences of the pressure from its mean value p_0 $[\mathbf{I}]$ (with $[\mathbf{I}]$ being the unit tensor), and \mathbf{v}_Γ as surface velocity, the integral representation from the FW-H formulation can be expressed as [21, 34]

$$\begin{aligned} \rho' &= \frac{1}{4\pi c_0^2} \nabla \cdot \nabla \cdot \int_{\Omega} \left[\frac{[\mathbf{L}]}{r[1 - Ma_r]} \right]_{\text{ret}} d\Omega \\ &\quad - \frac{1}{4\pi c_0^2} \nabla \cdot \int_{\Gamma} \left[\frac{[\mathbf{P}] \cdot \mathbf{n}}{r[1 - Ma_r]} \right]_{\text{ret}} d\Gamma \\ &\quad + \frac{1}{4\pi c_0^2} \frac{\partial}{\partial t} \int_{\Gamma} \left[\frac{\rho_0 \mathbf{v}_\Gamma \cdot \mathbf{n}}{r[1 - Ma_r]} \right]_{\text{ret}} d\Gamma. \end{aligned} \quad (3)$$

Furthermore, \mathbf{r} accounts for the vector from the surface to the observer, Ma_r for the Mach number in the direction of \mathbf{r} , and $[\mathbf{W}]_{\text{ret}}$ states that the terms are evaluated at retarded time. It is noted that the original formulation (3) only incorporates impermeable surfaces. By applying a more general formulation, we incorporate permeable surfaces and, as a result, neglect moving surfaces since the rotating impeller region can be omitted. This allows to cancel out the third part of equation (3), which considers moving surfaces. Furthermore, viscous stresses are neglected since they do not contribute significantly to such technical devices with high Reynolds numbers. Finally, this brings up [35]

$$\begin{aligned} \rho' &= \frac{1}{4\pi c_0^2} \nabla \cdot \nabla \cdot \int_{\Omega} \left[\frac{[\mathbf{L}]}{r[1 - Ma_r]} \right]_{\text{ret}} d\Omega \\ &\quad - \frac{1}{4\pi c_0^2} \nabla \cdot \int_{\Gamma} \left[\frac{([\mathbf{P}] + \rho \mathbf{v} \otimes \mathbf{v}) \cdot \mathbf{n}}{r[1 - Ma_r]} \right]_{\text{ret}} d\Gamma. \end{aligned} \quad (4)$$

The FW-H analogy implemented in Star-CCM+ v.12.06 is based on the free-field Green's function for computing pressure fluctuations at receiver points. For the simulations presented in this paper, the non-convective Dunn Farassat Padula 1A formulation [35] is considered. This formulation is specially designed for impermeable surfaces, which are part of subsonic rotating geometries [35, 36]. For including convective effects, an effective speed of sound incorporating the propagation speed of pressure waves with convective velocity effects [36]

$$c_\theta = \frac{c_0(1 - Ma^2)}{\sqrt{1 - Ma^2 \sin^2(\theta) + Ma \cos(\theta)}}, \quad (5)$$

is considered in the FW-H analogy. Thereby, θ denotes the angle between the convective velocity and the direction of propagation. Based on this implementation, restrictions for in-duct propagation simulation of turbocharger

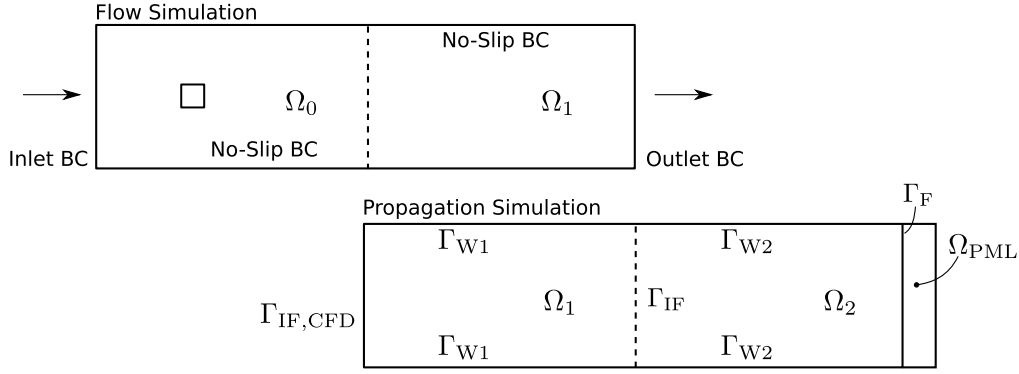


Figure 1. Computational domains for solving Lighthill's inhomogeneous wave equation, and the flow simulation depicting all boundaries.

compressors appear. Using source terms at permeable and impermeable surfaces for propagating pressure fluctuations, requires resolving all length and time scales. The Dunn Farassat Padula's 1A formulation is specially designed for subsonic rotating geometries [35]. However, with turbocharger compressors, the local Mach numbers “Ma” are larger than one, depending on the point of operation.

2.2 Finite element formulation of Lighthill's equation

Lighthill's wave equation (1), in combination with the FE method (LH-FE) provides an already given flow field established by the flow solver. As a result, boundary conditions connecting the flow simulation and the FE-based propagation simulation have to be established. In this sense, we consider the following boundary conditions connecting the flow simulation ($\Omega_f = \Omega_0 \cup \Omega_1$) and propagation simulation ($\Omega_p = \Omega_1 \cup \Omega_2$) (see Fig. 1):

- Interface boundary condition $\Gamma_{IF,CFD}$:
- The interface boundary separates the flow domain $\Omega_f = \Omega_0 \cup \Omega_1$ and, as a consequence, is not present in the flow simulation. For incorporating density fluctuations ρ' that propagate into Ω_1 via $\Gamma_{IF,CFD}$ an inhomogeneous Neumann boundary condition is applied

$$(\nabla \rho') \cdot \mathbf{n} = (\nabla \rho'_{CFD}) \cdot \mathbf{n}, \quad (6)$$

with ρ'_{CFD} as density fluctuations derived by the flow simulation.

- Wall boundaries incorporated in the flow simulation Γ_{W1} :

In the flow simulation, a non-moving and no penetration no-slip boundary ($\mathbf{v}_{Wall} = \mathbf{0}$) is applied at Γ_{W1} . Using conservation of momentum by neglecting external forces and considering the definition of Lighthill's stress tensor (2) brings up at Γ_{W1}

$$\nabla \cdot [\mathbf{L}] \cdot \mathbf{n} = -\nabla \cdot (c_0^2 \rho') \cdot \mathbf{n}. \quad (7)$$

Consequently, a homogeneous Neumann boundary condition

$$\nabla \rho' \cdot \mathbf{n} = 0, \quad (8)$$

is applied at Γ_{W1} .

- Wall boundaries not incorporated in the flow simulation at Γ_{W2} :

For wall boundaries not incorporated in the flow simulation, two possibilities are discussed. Firstly, assuming that aerodynamic and acoustic pressure fluctuation would exist at Γ_{W2} brings up the same consideration as for Γ_{W1} . Secondly, if only acoustic pressure fluctuations remain at Γ_{W2} a sound hard wall boundary condition can be applied, resulting in a homogeneous Neumann boundary condition [22]. Either way, a homogeneous Neumann boundary condition is considered for Γ_{W2} .

- An internal boundary condition Γ_{IF} :

A perfectly working outlet boundary condition of the flow simulation is assumed. In such cases, all radiating density fluctuations are damped away, and no reflections propagate back into Ω_2 . To avoid reflections at the outlet boundary condition, grid stretching or sponge layers can be applied [16]. As a result, Γ_{IF} has not to be incorporated into the propagation computation.

- A free propagation boundary condition Γ_F :

For incorporating free propagation at Γ_F , a PML technique [37] with an inverse distance damping function in time domain was applied by adding Ω_{PML} (see Fig. 1).

To obtain the weak formulation of Lighthill's equation (1), we multiply the partial differential equation with the test function $\varphi \in H_0^1$, integrate over the propagation domain Ω_p , and apply integration by parts to the Laplace term of the differential operator and the source term

$$\begin{aligned} & \int_{\Omega_p} \frac{1}{c_0^2} \varphi \frac{\partial^2}{\partial t^2} c_0^2 \rho' d\Omega + \int_{\Omega_p} \nabla c_0^2 \rho' \cdot \nabla \varphi d\Omega \\ & = \int_{\Gamma_p} (\nabla \cdot [\mathbf{L}] + \nabla c_0^2 \rho') \cdot \mathbf{n} \varphi d\Gamma - \int_{\Omega_p} \nabla \cdot [\mathbf{L}] \cdot \nabla \varphi d\Omega. \end{aligned} \quad (9)$$

Separating the boundaries according to $\Gamma_p = \Gamma_{\text{IF,CFD}} \cup \Gamma_{\text{W1}} \cup \Gamma_{\text{W2}} \cup \Gamma_F$ (see Fig. 1) and applying the corresponding boundary conditions brings up

$$\begin{aligned} & \int_{\Omega_p} \frac{1}{c_0^2} \varphi \frac{\partial^2}{\partial t^2} c_0^2 \rho' d\Omega + \int_{\Omega_p} \nabla c_0^2 \rho' \cdot \nabla \varphi d\Omega \\ &= \underbrace{\int_{\Gamma_{\text{IF,CFD}}} (\nabla \cdot [\mathbf{L}] + \nabla c_0^2 \rho') \cdot \mathbf{n} \varphi d\Gamma}_{\text{Surface Term}} - \underbrace{\int_{\Omega_1} \nabla \cdot [\mathbf{L}] \cdot \nabla \varphi d\Omega}_{\text{Volume Term}}. \end{aligned} \quad (10)$$

It is noted that the volume source term is only applied for Ω_1 since Ω_2 is not part of the flow simulation. Now, (2) is plugged into the surface term of (10) while the viscous stress term is neglected, bringing up

$$\begin{aligned} & \int_{\Omega_p} \frac{1}{c_0^2} \varphi \frac{\partial^2}{\partial t^2} c_0^2 \rho' d\Omega + \int_{\Omega_p} \nabla c_0^2 \rho' \cdot \nabla \varphi d\Omega \\ &= \underbrace{\int_{\Gamma_{\text{IF,CFD}}} (\nabla \cdot \rho \mathbf{v} \otimes \mathbf{v} + \nabla \cdot p[\mathbf{I}]) \cdot \mathbf{n} \varphi d\Gamma}_{\text{Surface Term}} - \underbrace{\int_{\Omega_1} \nabla \cdot [\mathbf{L}] \cdot \nabla \varphi d\Omega}_{\text{Volume Term}}. \end{aligned} \quad (11)$$

Consequently, the presented approach in its weak formulation, shows clear similarities with the approach of the FW–H analogy (4). However, due to the applied corresponding boundary conditions [38], solid surfaces are considered in (11) by applying homogeneous Neumann boundary conditions but have to be incorporated in the FW–H analogy (4) as source terms.

For applying LH-FE, the hybrid aeroacoustic workflow [39–43] is considered. The workflow can be separated into four different main steps [38]:

1. For computing aeroacoustic source terms, an unsteady flow simulation is performed.
2. The aeroacoustic source terms are interpolated from the flow to a propagation grid while conserving energy [41].
3. For performing the propagation simulation in the time domain, the source term mean part is filtered [44].
4. The propagation simulation is performed by using the open-source multiphysics FEM solver openCFS v.18.03 [45].

3 Simulation setups

For establishing all following results, a point of operation was used for which the “whooshing noise” could be verified with an engine test rig (see Tab. 1). The measurements from a cold gas test rig were used to validate simulation results [38, 46].

3.1 Flow simulation

As the first step, an unsteady and compressible flow simulation has been performed. Thereby, an Improved Delayed Detached Eddy Simulation (IDDES) with an underlying

Table 1. Point of operation used for all following measurements and simulations with n denoting the speed of rotation, PR denoting the pressure ratio, and \dot{m} denoting the mass flow rate.

n in 1/min	PR	\dot{m} in kg/s
88 740	1.7	0.12

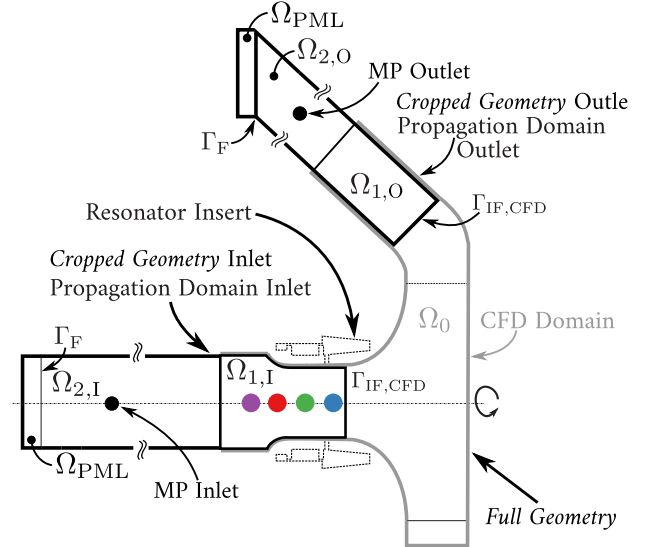


Figure 2. LH-FE setup for the *inlet* propagation region ($\Omega_{p,\text{Inlet}} = \Omega_{1,\text{I}} \cup \Omega_{2,\text{I}}$) and the *outlet* propagation region ($\Omega_{p,\text{Outlet}} = \Omega_{1,\text{O}} \cup \Omega_{2,\text{O}}$) with PML regions, and the FW–H setup showing both configurations, the *Cropped Geometries* and the *Full Geometry*. Also shown are evaluation points used in Figure 7.

k - ω SST turbulence model was considered [7]. A segregated flow solver with a hybrid second-order upwind/bounded-central scheme for convection was used. For turning the impeller region, a rigid body rotation was applied. The computation grid utilizes polyhedral cells with refinements at regions with high-velocity gradients, e.g. in the blade tip gap, and prism layers for the boundary layer were used. Considering a grid size of 1.6 mm in the inlet and outlet region and a grid size of 1.3 mm in the impeller region in combination with 10–18 prism layers brought up a grid with 22 417 322 cells. The used time step size corresponds to 1° of rotation of the impeller resulting in $\Delta t = 1.878 \times 10^{-6}$ s. In addition, for time-stepping a second-order implicit time-stepping scheme was used. The usage of an implicit temporal solver allows simulations of compressible flows with Courant–Friedrichs–Lewy (CFL) numbers [16, 33]

$$\text{CFL} = \frac{(|\mathbf{v}| + c) \Delta t}{\Delta x} \geq 1, \quad (12)$$

if the mean value is close to $\overline{\text{CFL}} \approx 1$, with Δx as local cell size. For the established grid, an averaged CFL number of 1.284 with a maximal value of $\text{CFL}_{\text{max}} = 86.39$ was obtained. Thereby, $\text{CFL} \leq 1$ holds for about 3.2%, and $\text{CFL} > 1$ for about 96.8% of all cells. As boundary conditions, a mass flow inlet and a pressure outlet were

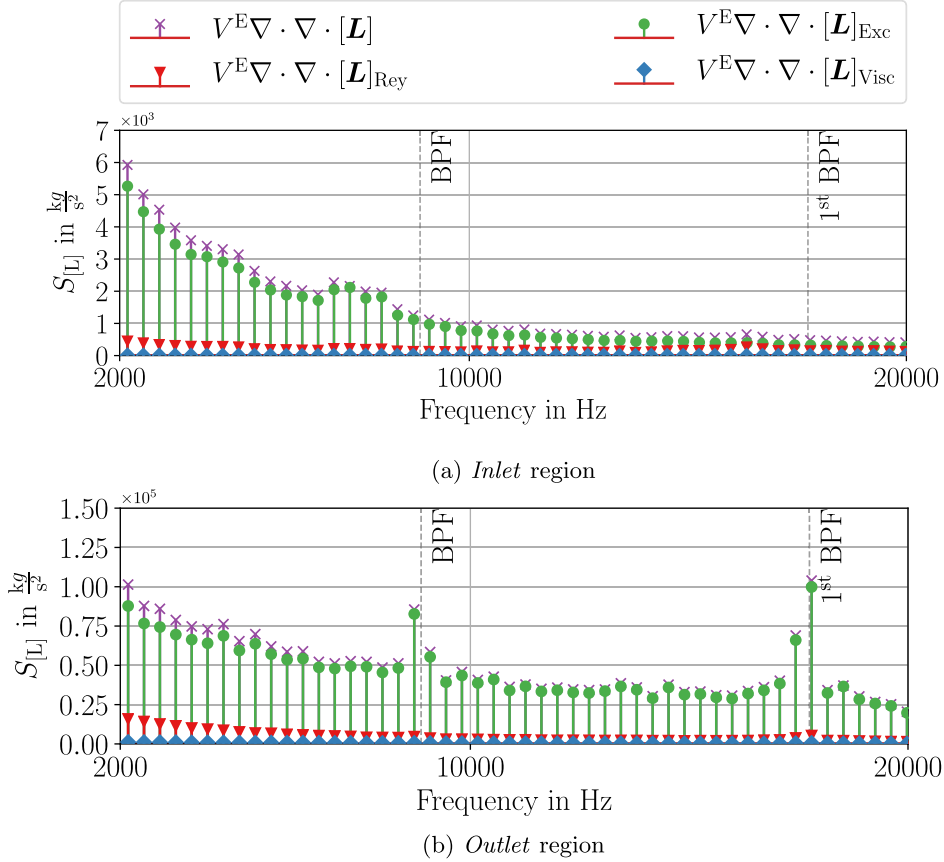


Figure 3. Sum of the absolute values of Lighthill's source term $\nabla \cdot \nabla \cdot [\mathbf{L}]$ and its three main parts of the *inlet* and *outlet* region. For processing data of $t = 0.00270453$ s, corresponding to 4 turns, and a Hamming window function was considered.

considered [16]. Furthermore, the all y^+ wall treatment was applied to address wall boundary layers. This approach automatically detects local y^+ values and applies the best fitting wall treatment. For this investigation a trade-off between grid size, y^+ values, and computational effort was considered, resulting in averaged y^+ values of around unity at the blades and overall averaged $y^+ \approx 7.9$ for the entire flow domain due to spatial coarsening in undisturbed regions. For varying y^+ values, the all y^+ wall treatment delivers adequate results [16, 17]. Furthermore, considering the surface averaged flow velocity \bar{v}_Γ at $\Gamma_{\text{IF,CFD}}$, as shown in Figure 2, brings up Reynolds numbers of $\text{Re}_{\text{In}} \approx 137 \times 10^3$ at the inlet, and $\text{Re}_{\text{Out}} \approx 187 \times 10^3$ at the outlet, respectively. For a detailed explanation of the used flow simulation setup, we refer to [38, 47].

In addition, all FW-H simulations were performed parallel to the flow simulation in Star-CCM+ v.12.06.

3.2 Propagation simulation

The propagation simulation setup for the LH-FE approach is generally different from the flow simulation setup. For performing a flow simulation, it is essential to resolve length and time scales of turbulent eddies. Consequently, spatial refinements in regions with, e.g. high-velocity gradients have to be applied. In contrast, the

propagation grid has to be uniform for adequate wave transportation to prevent numerical reflections in the propagation domain [22]. A common approach is to approximate the wavelength λ corresponding with the highest frequency of interest, with 10–20 finite elements [22, 40–43, 48]. For our computations, the frequency range of 1000 Hz to 20 000 Hz is of interest, bringing up

$$\lambda_{\min} = \frac{c}{f_{\max}} = \frac{341 \text{ m/s}}{20\,000 \text{ Hz}} = 1.705 \text{ mm}. \quad (13)$$

Based on [40, 41, 43, 48], we use 10 finite elements per wavelength for spatial discretization, arriving at a mesh resolution of

$$\Delta h = \frac{\lambda_{\min}}{10} = 0.0017 \text{ m} \triangleq 1.7 \text{ mm}. \quad (14)$$

Finally, the propagation grid is assessed by

$$\Delta h \leq \lambda_{\min}. \quad (15)$$

Using this propagation grid as target grid, source terms are interpolated applying the least square interpolation approach implemented in Star-CCM+ [49]. The accuracy of this interpolation approach was assessed by interpolating the pressure p_{CFD} established by the flow simulation onto the propagation grid resulting in p_p and computing a relative error

$$\epsilon = \sqrt{\frac{\left(\int_{\Omega_p} p_p d\Omega - \int_{\Omega_{CFD}} p_{CFD} d\Omega\right)^2}{\left(\int_{\Omega_{CFD}} p_{CFD} d\Omega\right)^2}}. \quad (16)$$

In (16) Ω_p denotes the propagation grid and Ω_{CFD} the flow grid. Furthermore, for this investigation, Ω_p and Ω_{CFD} were designed to be the same size and incorporated the *inlet* region. This investigation showed a relative error of $\epsilon \approx 8.65\%$ for the whole domain, which was in very good agreement with other interpolation algorithms [38].

Thereby, it is noted that during the interpolation from the flow to the propagation grid, only source terms of $\Omega_{1,w}$ are considered, neglecting source terms of Ω_0 . In the next step, the computed Lighthill's source terms, and its three parts are investigated for the *inlet* and *outlet* region of the propagation grid (see Fig. 2). Because of the introduced interface boundary condition $\Gamma_{IF,CFD}$, the computation of Lighthill's source term is restricted to parts of the *inlet* and *outlet* region (see Fig. 2). As a result, the source term interpolation is just performed for the *inlet* and *outlet* region. This allows reducing the amount of exported data significantly. Furthermore, the required simulation time of the LH-FE propagation computation decreases since smaller computation domains can be used. Consequently, the efficiency of the entire hybrid workflow increases, hence enabling to consider more time steps.

4 Results

Subsequently, an extensive source term investigation and results of the flow simulation, the LH-FE, and the FW-H propagation approach are shown and compared.

4.1 Source term investigation

For investigation, the cell-centroid-based source terms of a simulation time of 0.27 ms, which corresponds to four impeller turns, are weighted with the finite element volume V^E and transformed into the frequency domain while using a Hamming window function. The real and imaginary parts of the transformed source terms of the whole domain are summed up for each frequency, and the magnitude $S_{[L]}(f)$ is computed [50]

$$S_{[L]}(f) = \left[\left(\sum_{i=1}^{N^E} \Re(V_i^E \nabla \cdot \nabla \cdot [\hat{\mathbf{L}}]_i^E)(f) \right)^2 + \left(\sum_{i=1}^{N^E} \Im(V_i^E \nabla \cdot \nabla \cdot [\hat{\mathbf{L}}]_i^E)(f) \right)^2 \right]^{1/2}. \quad (17)$$

Investigating Lighthill's source term $\nabla \cdot \nabla \cdot [\mathbf{L}]$ (see Fig. 3a) in the *inlet* region (see Fig. 2) shows that the superposition of the three source term parts brings up a full Lighthill source term with amplitudes larger than the amplitudes of the three single parts. Furthermore, the parts

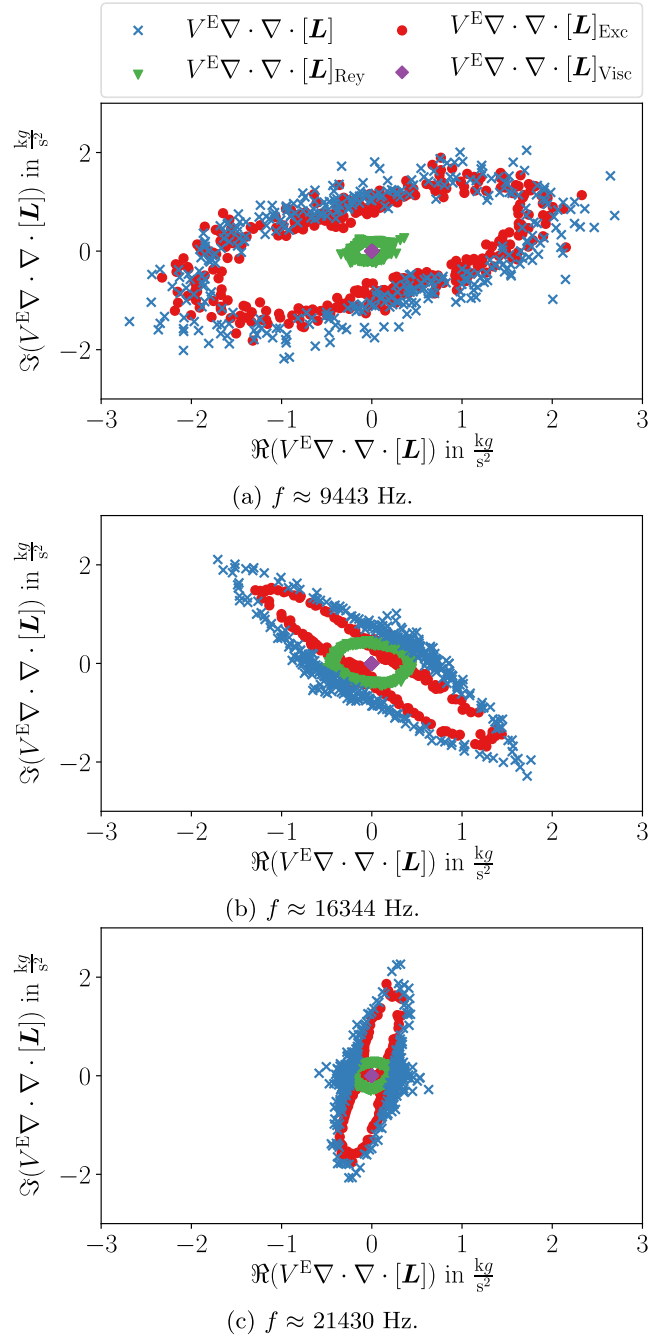


Figure 4. Lighthill's source term parts for different frequencies of the *inlet* region of $t = 0.00270453$ s, corresponding to 4 impeller turns.

due to the Reynold stresses and the viscous stresses are small compared to the dominant excess source term. This is interesting since, due to the low Mach number in the *inlet* region, a dominant Reynolds source term was expected. In the *inlet* region, an averaged Mach number $\overline{Ma} \approx 0.1$ was computed. As a result, this suggests a significant influence of the phases of the source term parts. Furthermore, since no source terms connected to the blade passing frequency (BPF) move far upstream into the *inlet* region, no dominant peaks can be seen. Investigating the source

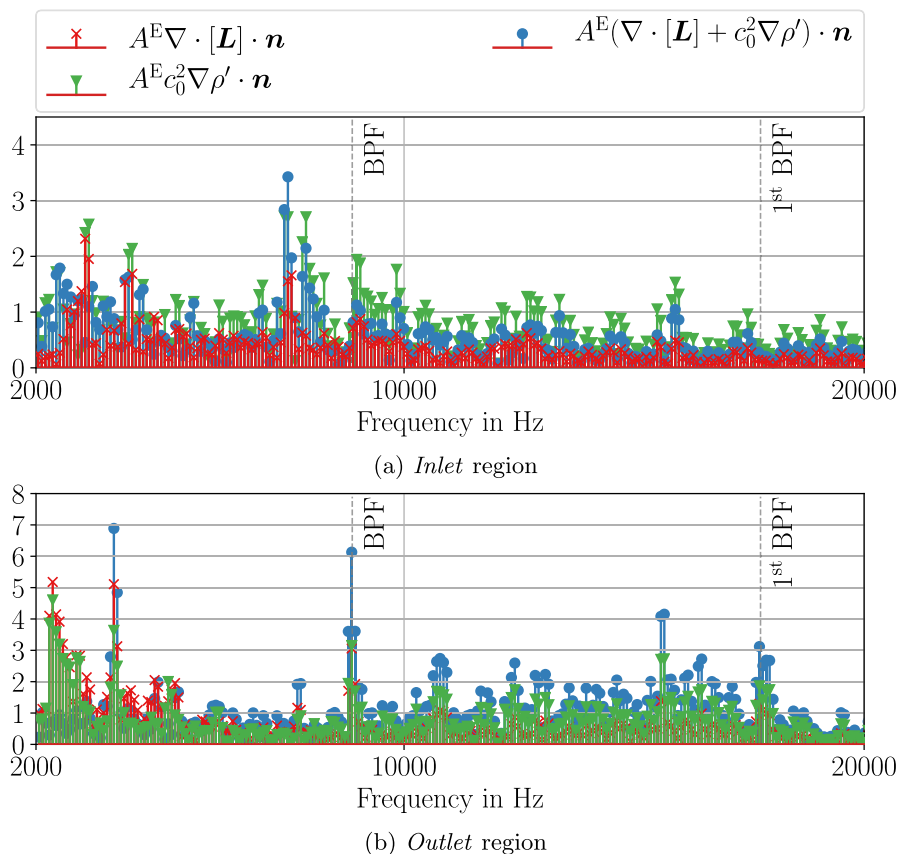


Figure 5. Surface weighted Lighthill source terms at the interface surface boundary $\Gamma_{\text{IF,CFD}}$ of the *inlet* and *outlet* region in the frequency domain of $t = 0.01352265$ s.

term $\nabla \cdot \nabla \cdot [\mathbf{L}]$ in the volume of the *outlet* region (see Fig. 3b) shows a similar pattern of the three Lighthill source term parts and their superposition. A higher influence of the excess term in the *outlet* region seems physical, since a higher averaged Mach number $\overline{\text{Ma}} \approx 0.16$ was computed. However, the large difference between the Reynolds and excess term again suggests a significant influence of the phases of the source term parts. For the *outlet* region, a dominant peak at the BPF and at the first harmonic of the BPF can be seen. This seems physical because source terms associated with the BPF originate in the impeller region and then travel downstream into the *outlet*. The slight shift between the actual peak at the BPF is connected to the coarse frequency resolution.

Due to the unexpected behaviour in the inlet, a more detailed investigation of the influence of the phase of Lighthill's source term parts is presented. Therefore, the real $\Re(\nabla \cdot \nabla \cdot [\mathbf{L}])$ and the imaginary $\Im(\nabla \cdot \nabla \cdot [\mathbf{L}])$ source term parts of each cell are used to compute the phase. Next, the real $\Re(\nabla \cdot \nabla \cdot [\mathbf{L}])$ and the imaginary $\Im(\nabla \cdot \nabla \cdot [\mathbf{L}])$ source term parts are weighted with the finite element volume V^E . Based on the phase ϕ , the weighted real $\Re(\nabla \cdot \nabla \cdot [\mathbf{L}])$ and the weighted imaginary $\Im(\nabla \cdot \nabla \cdot [\mathbf{L}])$ source term parts of all elements are sorted and summed up if they share a phase rounded to a full degree. Consequently, a summed up $\Re(\nabla \cdot \nabla \cdot [\mathbf{L}])(^\circ)$ and $\Im(\nabla \cdot \nabla \cdot [\mathbf{L}])(^\circ)$ for each full degree

of phase are brought up, showing, the energy for a certain phase in the entire domain. Investigating three different frequencies ($f_1 \approx 9443$ Hz, $f_2 \approx 16\,344$ Hz, $f_3 \approx 21\,430$ Hz) shows (see Fig. 4) that e.g., for $f \approx 21\,430$ Hz (see Fig. 4c) the energy of the Reynolds stress term in the *inlet* region is shifted by about 75° compared with the excess term. Consequently, depending on how dominant the excess term is compared to the Reynolds stress term, such a phase shift can bring up smaller amplitudes of the superposed full Lighthill's source term $\nabla \cdot \nabla \cdot [\mathbf{L}]$ for certain frequencies. In addition, investigating $f_1 \approx 9443$ Hz (see Fig. 4a) and $f_2 \approx 16\,344$ Hz (see Fig. 4b) shows that the phase shift between the excess and Reynolds stress term is not the same for different frequencies. Furthermore, for all presented investigations, the viscous stress term is small and can be neglected.

Considering the used weak formulation of Lighthill's equation (10), we furthermore investigate the two different source term parts, $\nabla \cdot [\mathbf{L}] \cdot \mathbf{n}$ and $c_0^2 \nabla \rho' \cdot \mathbf{n}$ as well as their superposition at $\Gamma_{\text{IF,CFD}}$ of the *inlet* and *outlet* region. Hereinafter source terms located at $\Gamma_{\text{IF,CFD}}$ are referred to as surface source terms. It is mentioned that $\nabla \cdot [\mathbf{L}] \cdot \mathbf{n}$ incorporates source term parts that arise at $\Gamma_{\text{IF,CFD}}$. The second part $c_0^2 \nabla \rho' \cdot \mathbf{n}$ incorporates density fluctuations ρ' which propagate into the domain by $\Gamma_{\text{IF,CFD}}$. Consequently, both source term parts incorporate the influence

of the omitted geometries. For investigating the source term parts at $\Gamma_{\text{IF,CFD}}$, the surface weighted surface source terms are summed up for $1000 \text{ Hz} \leq N^f < 20\,000 \text{ Hz}$

$$S_{\text{IF,CFD}} = \sum_{j=1}^{N^f} \left(\sum_{i=1}^{N^E} (A_i^E W_{i,j}) \right), \quad (18)$$

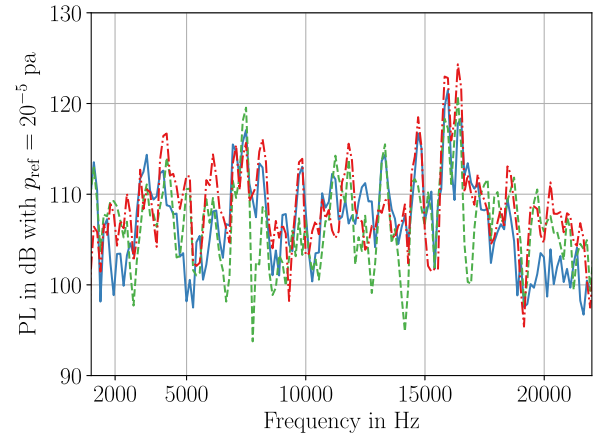
with W as $\nabla \cdot [\mathbf{L}] \cdot \mathbf{n}$, $c_0^2 \nabla \rho' \cdot \mathbf{n}$, and $(\nabla \cdot [\mathbf{L}] + c_0^2 \nabla \rho') \cdot \mathbf{n}$. Thereby, it could be shown that for $\Gamma_{\text{IF,CFD}}$ for the *inlet* region, the term $c_0^2 \nabla \rho' \cdot \mathbf{n}$ is dominant (see Fig. 5). Furthermore, it could be shown that at the interface, local peaks connected with the BPF appear. This sounds physical since $\Gamma_{\text{IF,CFD}}$ is located close to the impeller, and density fluctuations arising in the impeller propagate a small distance upstream for this point of operation. Investigating surface source terms at $\Gamma_{\text{IF,CFD}}$ of the *outlet* regions shows that both source term parts, $\nabla \cdot [\mathbf{L}] \cdot \mathbf{n}$ and $c_0^2 \nabla \rho' \cdot \mathbf{n}$ are of a similar order. Furthermore, a clear peak at the BPF can be seen. Density fluctuations connected with the BPF originate directly after the impeller and propagate further downstream. The interface of the *outlet* region is located downstream of the outlet volute, which is why strong density fluctuations connected with the BPF propagate into the *outlet* region via $\Gamma_{\text{IF,CFD}}$.

4.2 Propagation results

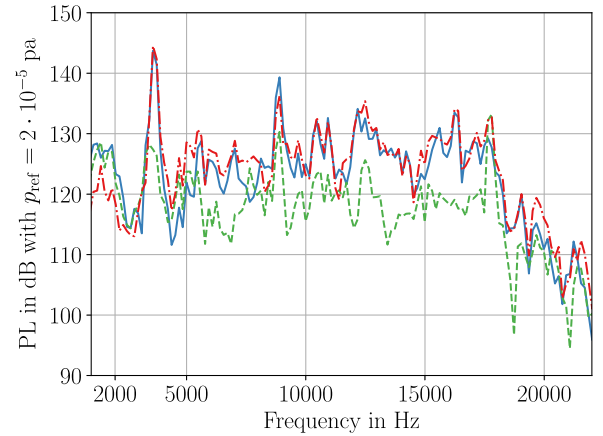
Finally, the presented Lighthill's source terms are considered for solving the LH-FE propagation [45]. Therefore, a time step size of $\Delta t_{\text{prop}} = 5 \cdot 10^{-6} \text{ s}$ was used. Furthermore, the ideal gas law was considered for computing pressure fluctuations p' based on the density fluctuations ρ' in the isentropic far-field. Therefore, a constant temperature T was taken into account, which is the middle part of the temperature T simulated by the flow solver at the evaluation points *MP Inlet* and *MP Outlet*. Furthermore, for smoothly plugging in source terms in the propagation computation a temporal blending function

$$f_{t,B} = \begin{cases} \cos\left(\frac{\pi}{2t_{\text{lim}}}(t - t_{\text{lim}})\right)^2 & t < t_{\text{lim}} \\ 1 & t > t_{\text{lim}} \end{cases}, \quad (19)$$

with $t_{\text{lim}} = \Delta t \cdot n$, and $n = 200$ steps was applied to avoid transient effects in the solution [43]. As shown in Figure 2, volume source terms are only available for a part of the considered propagation domains ($\Omega_{1,W}$) of the *inlet* and *outlet* region. As the first step, the individual contribution of surface source terms of $\Gamma_{\text{IF,CFD}}$, the volume source terms, and both of those source terms at once are investigated by performing propagation simulations. Thereby, it could be shown that the volume source term is dominant (see Fig. 6) for the *outlet* region and contributes significantly for the *inlet* region. The influence of the surface source term, especially in the *outlet* region, is comparatively small compared to a strong influence in the *inlet* region since in the outlet region strong source terms appear in the volume as well due to downstream traveling source terms. Furthermore, investigating results of the



(a) *MP Inlet 1*



(b) *MP Outlet 1*

Figure 6. The influence of full source terms (—), surface source terms (---), and the volume source terms (— · —) considering a simulation time of $t = 0.01352265 \text{ s}$, corresponding to 20 turns. For performing an FFT for simulation results the time signals were separated into three parts with 30% overlap, and a Hamming window function was used. This results in a frequency resolution of about $\Delta f = 160 \text{ Hz}$.

outlet region, shows that the transversal mode located at $f_{Q,1} = 3672 \text{ Hz}$ is mainly excited by the volume source terms, since they are distributed over a larger region. In contrast, surface source terms located at $\Gamma_{\text{IF,CFD}}$ can not similarly excite transversal modes. In the turbocharger compressor, strong turbulent eddies are generated in the impeller and, for points of operation close to the design point, travel with the flow in the *outlet* region. For points of operation close to the surge line, noteworthy turbulent eddies, and as a result, noteworthy Lighthill source terms, also travel from the *impeller* region upstream into the *inlet* region. Therefore, it is noted that the described influences of surface and volume source terms may vary for different points of operations. E.g., points of operation with stronger backflow throughout the *impeller* into the

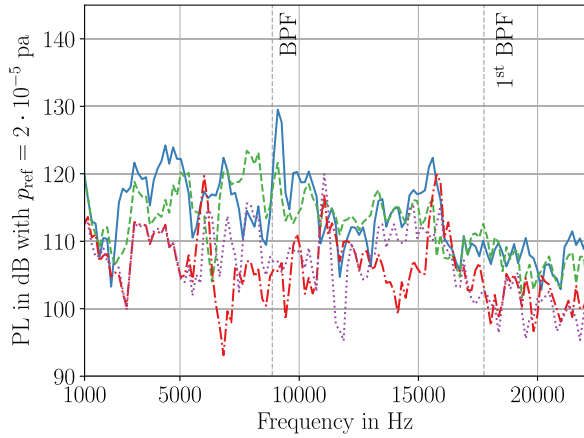
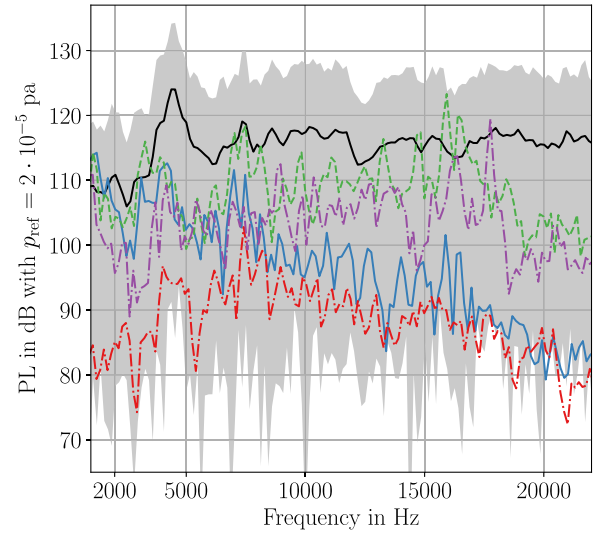


Figure 7. Pressure fluctuations established by the CFD evaluated at four different points, considering a simulation time of 0.01352265 s, which corresponds to 20 turns. Evaluation points are located in the longitudinal axis of the inlet, and their position is defined by referring to the impeller hub. The evaluation points are located $x/D_W = 0.08$ (—), $x/D_W = 0.81$ (---), $x/D_W = 1.62$ (-.-), and $x/D_W = 2.42$ (···) with D_W as the duct diameter. For postprocessing, the signal was separated into five different blocks with 45% overlap and a Hamming window function was used. This results in a frequency resolution of about $\Delta f \approx 150$ Hz.

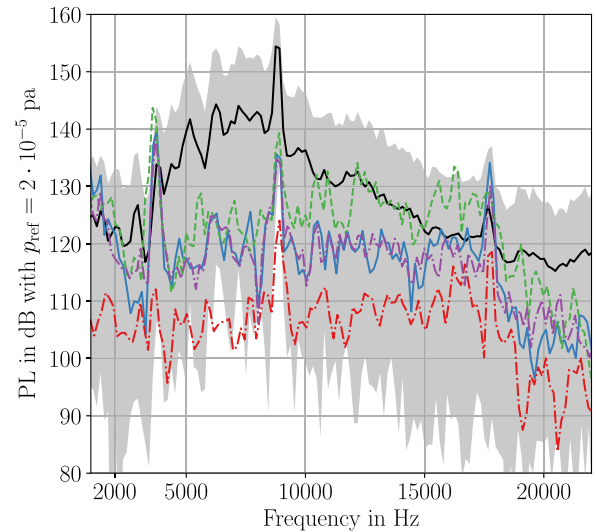
inlet region show different flow characteristics, and the influence of the volume source may further increase. However, the source terms at the interface boundary condition contain not just source terms located exactly at $\Gamma_{IF,CFD}$ (by incorporating $\nabla \cdot [\mathbf{L}] \cdot \mathbf{n}$) but also density fluctuations propagating from the impeller into the *inlet* region (by incorporating $c_0^2 \nabla \rho' \cdot \mathbf{n}$). Consequently, if $\Gamma_{IF,CFD}$ is located in a way that no significant Lighthill source terms remain but just density fluctuations, the surface source term will be dominant. Concluding, it can not be said in general which of the source terms, the one located in the volume or at the interface boundary condition, are the most dominant. However, if the fluid is quiescent, no source terms appear and $c_0^2 \nabla \rho' \cdot \mathbf{n}$ will be dominant.

For computing FW–H propagation results, two different setups were considered (see Fig. 2). The setup *Full Geometry* considers all impermeable surfaces of the turbocharger compressor. The setup *Cropped Geometry* considers all impermeable and permeable surfaces corresponding to the surfaces of the *inlet* and *outlet* propagation domain used for LH-FE (see Fig. 2). It is noted that the *Cropped Geometry* setup neglects all areas with $Ma > 1$ appearing in the impeller region, which are included in the *Full Geometry*.

Investigating the results from the flow simulation, LH-FE, and the FW–H analogy by comparing them with measurements from the cold gas test rig shows that FW–H of the *Cropped Geometry* significantly underestimates amplitudes for both, the *inlet* (see Fig. 8a) and *outlet* (see Fig. 8b) regions. Furthermore, it can be seen that flow simulation results are strongly influenced by numeric dissipation [17, 38]. Especially for the evaluation point of the *inlet* region, amplitudes for higher frequencies are damped.



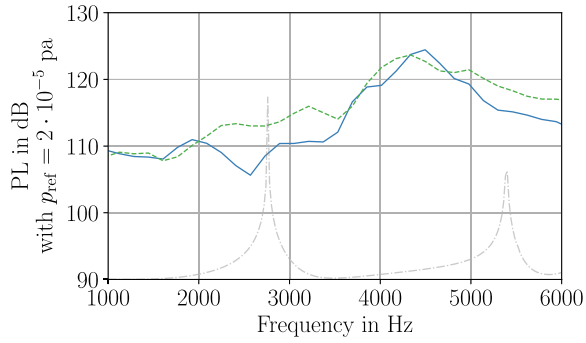
(a) *MP Inlet 1*



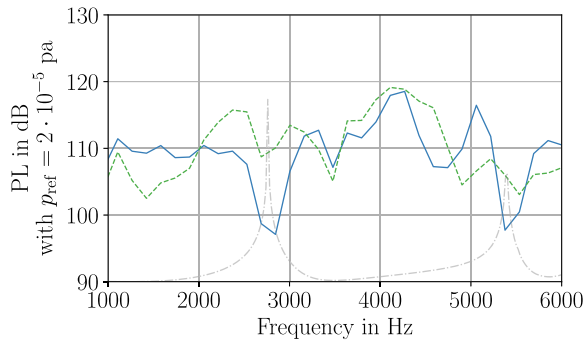
(b) *MP Outlet 1*

Figure 8. Propagation results established using FW–H analogy for the cropped geometry (---), the full geometry (···), and the LH-FE approach (---) compared with flow simulation results (—) at *MP Inlet 1* and *MP Outlet 1* for a computational time of 0.01352265 s, corresponding to 20 turns. For postprocessing, the time signal was separated into 3 blocks with 30% overlap, and a Hamming window function was applied. For postprocessing, the measurement (—) $t_{meas} = 10$ s was separated into 2620 parts (—) with an overlap of 30% and also a Hamming window function. This brought up a frequency resolution of $\Delta f \approx 150$ Hz.

The evaluation point of the *inlet* region is more influenced than the evaluation point of the *outlet* region because it is further away from the impeller, where most of the source terms are generated. In addition, the differences between results of the flow simulation and the LH-FE of the *outlet* region are small since the considered source terms of the *outlet* region propagate far downstream, which is why they



(a)



(b)

Figure 9. Measurement and simulation results showing the influence of the used resonator insert (—) comparing with a closed resonator (---) at the evaluation point *MP Inlet 1* in the *inlet* region. For both simulations a frequency resolution of about $\Delta f \approx 160$ Hz have been achieved. The characteristic TL of the resonator insert is depicted in (---). (a) Measurement results without resonator insert for $t = 10$ s. For postprocessing, the time signal was split into 2700 blocks with 30% overlap and a Hamming window function was used. (b) Lighthill's propagation results with open and closed resonator insert. For performing an FFT for the Lighthill propagation, the time signal of 20 turns was separated into 3 parts with 30% overlap, and a Hamming window function was used.

are also influenced by numeric dissipation. It is noted that *MP Inlet* is located 0.34 m away from the source terms of the impeller region. The distance between *MP Outlet* and source terms can not easily be assessed. Strong source terms are mainly generated in the impeller region and propagate further downstream. As a result, significant source terms can be found in a large area of the impeller, outlet volute, and even the *outlet* region, making it challenging to define their distance to evaluation points. Furthermore, this shows that source terms, especially in the *outlet* region, are also influenced by numeric dissipation.

Furthermore, it can be seen that FW–H for the *Full Geometry* setup delivers results with amplitudes of similar order than results established using LH-FE for the *inlet* (see Fig. 8a) and *outlet* (see Fig. 8b) region, and furthermore both are in good agreement with measurements.

Table 2. Comparison of required computation times of the flow (IDDES) simulation, the LH-FE approach, and the FW–H analogy for the full (f) and cropped (c) geometries.

Case	Cluster	nCores	Wall times
IDDES	VSC	2×24	~504 h
LH-FE	RK3	1×8	~10 h
FW–H (f & c)	Parallel to flow simulation		

Table 3. Estimated time required for computing a propagation simulation for an additional resonator geometry using the LH-FE approach.

Estimated expenditure of time of LH-FE	
Work step	Duration (h)
Generate new propagation mesh	0.50
Interpolation (only surface terms)	0.05
Propagation simulation	9.50
Investigation results	0.05
	$\Sigma = 10.10$

The result of the FW–H analogy for the *Full Geometry* setup shows that in the *inlet* region the BPF ($f_{\text{BPF}} = 8874$ Hz) and its first harmonic ($f_{\text{BPF},1} = 17\,748$ Hz) are resolved. To validate this assumption, pressure fluctuations p' derived from the flow simulations at four different evaluation points located in the *inlet* region are investigated (see Fig. 7). The four evaluation points are placed at the central axis of the inlet and are located between 0.08 and 2.42 times the duct diameter D_W away from the impeller hub. The spectrum of those pressure fluctuations (see Fig. 7) shows that the BPF can only be seen at the closest two evaluation points, located 0.08 m and 0.81 times D_W away from the impeller hub. Consequently, since the considered evaluation point for the FW–H simulations is much further away from the impeller hub, it seems unphysical that the BPF and its first harmonic is that dominant in results established for the *inlet* region since this can not be seen in measurements. Furthermore, the slight frequency shift from the peak connected with the BPF investigated in Figure 7 is connected with the Doppler effect because the main Lighthill source terms are generated at the impeller blades and move further downstream.

Furthermore, the dominant peak of about 3680 Hz that can be seen for simulation results established in the *outlet* region (see Fig. 8b), which is not equally dominant in measurements, can be connected with a transversal mode.

The presented LH-FE approach and the FW–H analogy enable propagating pressure fluctuations based on source terms established by compressible flow simulations. The FW–H analogy is especially efficient in computing pressure fluctuations at discrete receiver points. In contrast, LH-FE efficiently computes pressure fluctuations for the whole propagation domain. As a result, for computing coupled vibro-acoustic simulations, the FW–H analogy would have to be performed multiple times for a high number of

Table 4. Computational resources used for LH-FE simulations.

Compute Server RK 3	
CPU	Intel/(R) Xeon (R) Gold 5218 CPU @ CPU 2.30 GHz 2 physical processors; 32 cores; 64 threads
RAM	DDR4 756 GB with 2933 MHz
Storage	SAS HDDs mit 10000 rpm im Raid 5.0 with averaged read rate of 490 MB/s and averaged write rate of 284 MB/s
Operation System	Ubuntu 20.04.3 LTS

receiver points. For such applications, the LH-FE approach seems more suitable.

4.3 Practical aspects

In a next step, investigate the practical aspects of the presented LH-FE approach. As can be seen in [Figure 2](#), a resonator insert as part of the inlet region is used. This resonator geometry is characterized by the transmission loss (TL), which was investigated in detail in [\[20\]](#). Let's now consider the TL of the used resonator insert, which has two maxima, one at $f_{TL,max1} \approx 2600$ Hz, and one at $f_{TL,max2} \approx 5400$ Hz.

Investigating measurements from the cold gas test rig at *MP Inlet 1* clearly shows (see [Fig. 9a](#)) significantly smaller amplitudes in areas around the maxima of the TL of the resonator insert. To investigate if the presented LH-FE approach can simulate the influence of the resonator insert in a similar way, source terms of the *inlet* region are considered.

Since in the *inlet* region, the surface source terms located at $\Gamma_{IF,CFD}$ are in good agreement with results established by volume and surface source terms for the frequency range of interest (see [Fig. 6a](#)), the volume source terms are neglected for the following investigation. Only considering surface source terms allows a faster computation of the LH-FE approach. Surface source terms of $\Gamma_{IF,CFD}$ of one flow simulation are interpolated onto two different propagation grids, one including and one neglecting the resonator insert. Performing propagation simulations for those two different propagation setups also clearly show the influence of the resonator insert (see [Fig. 9b](#)). Comparing the results established by the cold gas test rig measurement (see [Fig. 9a](#)) and by the introduced LH-FE approach (see [Fig. 9b](#)) shows a similar influence of the resonator insert.

FW-H's analogy is not suitable for assessing different in-duct resonators and sound absorbers since source terms at impermeable surfaces are fundamental. In contrast, the LH-FE approach enables to neglect all impermeable surfaces and, as a result, is well suited for assessing different geometries based on one flow simulation.

Performing an enhanced flow simulation as presented, establishing converged results, and exporting source terms of at least 20 impeller turns took more than 3 weeks of extensive computations on the Vienna Scientific Cluster [\[51\]](#), using 2 nodes with 24 physical cores (see [Tab. 2](#)). Consequently, computing different flow simulations to investigate the influence of resonator inserts will take a

lot of time and will still be influenced by numeric dissipation. However, performing a propagation simulation based on the LH-FE approach took about 10 h to compute (see [Tab. 2](#)) using 8 cores at our RK3 compute server (see [Tab. 4](#)). A detailed representation of the required computing time of the individual steps can be seen in [Table 3](#). Consequently, the presented LH-FE approach gives a time advantage of about 50 times compared to performing an additional flow simulation.

5 Conclusions

A new FEM approach of Lighthill's wave equation for compressible flow simulations (LH-FE) incorporating interface boundary conditions for omitting geometry parts is investigated and compared with FW-H for turbocharger acoustic simulations. Analyzing Lighthill's aeroacoustic source terms in the *inlet* region, it could be shown that the volume source terms show no dominant influence at the BPF mechanism. In contrast, in the *outlet* region, the most dominant volume source terms are at the BPF. Furthermore, it is shown that Lighthill's source terms in the volume can be phased out. Depending on the flow simulation, this can lead to canceling out of different Lighthill's source term parts (Reynolds stress part, excess part, viscous stress part). Furthermore, it could be shown that depending on the location of the interface boundary condition, the influence of source terms of the volume or the surfaces varies substantially. Directly comparing results obtained by using the LH-FE approach and the FW-H analogy shows that for both propagation regions, the *inlet* and *outlet* region, the LH-FE approach is superior. However, if FW-H is applied to the whole turbocharger geometry, results are similar. In addition, it could be demonstrated that both sound propagation approaches are not influenced by numeric dissipation such as flow simulation results. However, based on the hybrid aeroacoustic workflow used for the LH-FE approach back-coupling is neglected. Furthermore, the approach requires a fine flow grid solution for the source term regions of the cropped geometries. Consequently, flow grids tend to consist of more cells than usually. Finally, the influence of a resonator insert was taken into account by considering its transmission loss and investigating its influence in measurements and simulations using the LH-FE approach. It could be shown that the LH-FE approach can represent the influence of the resonator insert by just using source terms of one flow simulation. Consequently,

the presented LH-FE approach is about 50 times faster for assessing the influence of resonators compared with flow simulations.

Conflict of interest

The authors declare no conflict of interest.

Acknowledgments

This research was funded by the bridge project with number 867971 of the Austrian Research Promotion Agency (FFG).

References

1. A. Gupta, A. Gupta, K. Jain, S. Gupta: Noise pollution and impact on children health. *The Indian Journal of Pediatrics* 85, 4 (2018) 300–306. <https://doi.org/10.1007/s12098-017-2579-7>.
2. D. Jhanwar: Noise pollution: a review. *Journal of Environment Pollution and Human Health* 4, 3 (2016) 72–77. <https://doi.org/10.12691/jephh-4-3-3>.
3. E. Commission: Amending Directive 2007/46/ec and Repealing Directive 70/157/eec. <https://eur-lex.europa.eu/LexUriServ/LexUriServ.do?uri=OJ:L:2007:263:0001:0160:en:PDF>.
4. United Nations: Sustainable development goals. <https://sdgs.un.org/goals>.
5. A. Mathur, H. Uitslag-Doolaard, F. Roelofs: Reduced-resolution RANS approach to grid spacer fuel assemblies. *Nuclear Engineering and Design* 356 (2020) 110374. <https://doi.org/10.1016/j.nucengdes.2019.110374>.
6. E.S. Oran, J.P. Boris: Computing turbulent shear flows – a convenient conspiracy. *Computers in Physics* 7, 5 (1993) 523–533. <https://doi.org/10.1063/1.4823213>.
7. F. Mendonca, O. Baris, G. Capon: Simulation of Radial Compressor Aeroacoustics Using CFD, in Proceedings of the ASME Turbo Expo 2012: Turbine Technical Conference and Exposition. Volume 8: Turbomachinery, Parts A, B, and C, June 11–15, 2012, Copenhagen, Denmark, 2012, 1823–1832. <https://doi.org/10.1115/GT2012-70028>.
8. J. Galindo, A. Tiseira, R. Navarro, M. López: Influence of tip clearance on flow behavior and noise generation of centrifugal compressors in near-surge conditions. *International Journal of Heat and Fluid Flow* 52 (2015) 129–139. <https://doi.org/10.1016/j.ijheatfluidflow.2014.12.004>.
9. A. Broatch, J. Galindo, J. Navarro, J. García-Tíscar: Methodology for experimental validation of a cfd model for predicting noise generation in centrifugal compressors. *International Journal of Heat and Fluid Flow* 50 (2014) 134–144. <https://doi.org/10.1016/j.ijheatfluidflow.2014.06.006>.
10. A. Broatch, J. Galindo, R. Navarro, J. García-Tíscar: Simulations and measurements of automotive turbocharger compressor whoosh noise. *Engineering Applications of Computational Fluid Mechanics* 9, 1 (2015) 12–20. <https://doi.org/10.1080/19942060.2015.1004788>.
11. A. Broatch, J. Galindo, R. Navarro, J. García-Tíscar: Numerical and experimental analysis of automotive turbocharger compressor aeroacoustics at different operating conditions. *International Journal of Heat and Fluid Flow* 61 (2016) 245–255. <https://doi.org/10.1016/j.ijheatfluidflow.2016.04.003>.
12. A. Broatch, J. García-Tíscar, F. Roig, S. Sharma: Dynamic mode decomposition of the acoustic field in radial compressors. *Aerospace Science and Technology* 90 (2019) 388–400. <https://doi.org/10.1016/j.ast.2019.05.015>.
13. S. Fontanesi, S. Paltrinieri, G. Cantore: CFD analysis of the acoustic behavior of a centrifugal compressor for high performance engine application. *Energy Procedia* 45 (2014) 759–768. <https://doi.org/10.1016/j.egypro.2014.01.081>.
14. R. Dehner, A. Selamet: Prediction of broadband noise in an automotive centrifugal compressor with three-dimensional computational fluid dynamics detached eddy simulations. *SAE International Journal of Advances and Current Practices in Mobility* 1 (2019) 1714–1720. <https://doi.org/10.4271/2019-01-1487>.
15. V. Jyothishkumar, M. Mihaescu, B. Semlitsch, L. Fuchs: Numerical flow analysis in centrifugal compressor near surge condition, in: 43rd AIAA Fluid Dynamics Conference, 2013, p. 2730. <https://doi.org/10.2514/6.2013-2730>.
16. E. Sundström, Flow instabilities in centrifugal compressors at low mass flow rate, Doctoral Thesis in Engineering Mechanics, KTH Stockholm, 2017.
17. E. Sundström, B. Semlitsch, M. Mihăescu: Acoustic signature of flow instabilities in radial compressors. *Journal of Sound and Vibration* 434 (2018) 221–236. <https://doi.org/10.1016/j.jsv.2018.07.040>.
18. E. Sundström, M. Mihaescu: Centrifugal compressor: The sound of surge, in 21st AIAA/CEAS Aeroacoustics Conference, 22–26 June, 2015, Dallas, Texas, USA, 2674. <https://doi.org/10.2514/6.2015-2674>.
19. B. Semlitsch, V. Jyothishkumar, M. Mihaescu, L. Fuchs: Investigation of the surge phenomena in a centrifugal compressor using large eddy simulation, in Proceedings ASME, 15–21 November, 2013, San Diego, California, USA. <https://doi.org/10.1115/IMECE2013-66301>.
20. A. Hauser: Numerical and experimental investigations on resonators in automotive air ducts, Master's Thesis, Technical University of Vienna, 2021.
21. J.E. Ffowcs Williams, D.L. Hawkings: Sound generation by turbulence and surfaces in arbitrary motion. *Philosophical Transactions of the Royal Society of London: Series A, Mathematical and Physical Sciences* 264, 1151, 1969, 321–342. <https://doi.org/10.1098/rsta.1969.0031>.
22. M. Kaltenbacher: Numerical simulation of mechatronic sensors and actuators: finite elements for computational multiphysics. 3rd ed., Springer, 2015.
23. M. Kaltenbacher, M. Escobar, S. Becker, I. Ali: Numerical simulation of flow-induced noise using LES/SAS and Lighthill's acoustic analogy. *International Journal for Numerical Methods in Fluids* 63 (2010) 1103–1122. <https://doi.org/10.1002/flid.2123>.
24. M. Tautz, K. Besserer, S. Becker, M. Kaltenbacher: Source formulations and boundary treatments for Lighthill's analogy applied to incompressible flows, *AIAA Journal* 56, 7 (2018) 2769–2781. <https://doi.org/10.2514/1.J056559>.
25. M. Escobar: Finite element simulation of flow-induced noise using Lighthill's acoustic analogy, Ph.D. Thesis, FAU Erlangen, 2007.
26. S. Caro, P. Ploumhans, X. Gallez, R. Sandboge, F. Sahkib, M. Matthes: A NEW CAA formulation based on Lighthill's analogy applied to an idealized automotive HVAC blower using AcuSolve and Actran/LA, in 11th AIAA/CEAS Aeroacoustics Conference, 23–25 May, 2005, Monterey, California, USA. <https://doi.org/10.2514/6.2005-3015>.
27. M.J. Lighthill: On sound generated aerodynamically. I. General theory. *Proceedings of the Royal Society* 211 (1952) 564–587. <https://doi.org/10.1098/rspa.1952.0060>.
28. M.J. Lighthill: On sound generated aerodynamically. II. Turbulence as a source of sound. *Proceedings of the Royal Society* 222 (1954) 1–32. <https://doi.org/10.1098/rspa.1954.0049>.

29. J.R. Ristorcelli: A closure for the compressibility of the source terms in Lighthill's acoustic analogy. ICASE Report.
30. R. Ewert: A hybrid computational aeroacoustic method to simulate airframe noise, Ph.D. thesis, Technische Hochschule Aachen, 2002.
31. M. Cabana, V. Fortuné, P. Jordan: Identifying the radiating core of Lighthill's source term. *Theoretical and Computational Fluid Dynamics* 22 (2008) 87–106. <https://doi.org/10.1007/s00162-008-0075-4>.
32. T. Colonius, J. Freund: Application of Lighthill's equation to a mach 1.92 turbulent jet. *AIAA Journal* 38, 2 (2000) 368–370. <https://doi.org/10.2514/2.966>.
33. C. Junger: Computational aeroacoustics for the characterization of noise sources in Rotatin systems, Ph.D. Thesis, TU Wien, 2019.
34. F. Farassat: Linear acoustic formulas for calculation of rotating blade noise. *AIAA Journal* 19, 9 (1981) 1122–1130. <https://doi.org/10.2514/3.60051>.
35. F. Farassat, S. Padula, M. Dunn: Advanced turboprop noise prediction based on recent theoretical results. *Journal of Sound and Vibration* 119, 1 (1987) 53–79. [https://doi.org/10.1016/0022-460X\(87\)90189-1](https://doi.org/10.1016/0022-460X(87)90189-1).
36. STAR-CCM+ documentation – Steve Portal, <https://the-steveportal.plm.automation.siemens.com>, accessed: 2019–05.
37. B. Kaltenbacher, M. Kaltenbacher, I. Sim: A modified and stable version of a perfectly matched layer technique for the 3-D second order wave equation in time domain with an application to aeroacoustics, *Journal of Computational Physics* 235 (2013) 407–422. <https://doi.org/10.1016/j.jcp.2012.10.016>.
38. C. Freidhager: Aeroacoustics of automotive turbochargers, Ph.D. Thesis, TU Graz, 2022.
39. S. Schoder, M. Kaltenbacher: Hybrid aeroacoustic computations: State of art and new achievements. *Journal of Theoretical and Computational Acoustics* 27, 04 (2019) 1950020. <https://doi.org/10.1142/S2591728519500208>.
40. S. Schoder, M. Weitz, P. Maurerlehner, A. Hauser, S. Falk, S. Kniesburges, M. Döllinger, M. Kaltenbacher: Hybrid aeroacoustic approach for the efficient numerical simulation of human phonation. *The Journal of the Acoustical Society of America* 147, 2 (2020) 1179–1194. <https://doi.org/10.1142/S2591728519500208>.
41. S. Schoder, A. Wurzinger, C. Junger, M. Weitz, C. Freidhager, K. Roppert, M. Kaltenbacher: Application limits of conservative source interpolation methods using a low mach number hybrid aeroacoustic workflow. *Journal of Theoretical and Computational Acoustics* 29, 1 (2021) 2050032. <https://doi.org/10.1142/S2591728520500322>.
42. S. Schoder, K. Roppert, M. Weitz, C. Junger, M. Kaltenbacher: Aeroacoustic source term computation based on radial basis functions. *International Journal for Numerical Methods in Engineering* 121, 9 (2020) 2051–2067. <https://doi.org/10.1002/nme.6298>.
43. S. Schoder, C. Junger, M. Kaltenbacher: Computational aeroacoustics of the eaa benchmark case of an axial fan. *Acta Acustica* 4, 5 (2020) 22. <https://doi.org/10.1051/aacus/2020021>.
44. C. Bogey, C. Bailly, D. Juvé: Computation of flow noise using source terms in linearized euler's equations. *AIAA Journal* 40, 2 (2002) 235–243. <https://doi.org/10.2514/6.2000-2047>.
45. openCFS: Finite elements for computational multiphysics. www.opencfs.org.
46. J.K. Müller: Zur Schallabstrahlung des Abgasturboladers in Abhängigkeit der Verdichter- und Turbinenansströmung, Ph.D. thesis, FAU Erlangen, 2020.
47. C. Freidhager, P. Maurerlehner, K. Roppert, M. Heinisch, A. Renz, S. Schoder, M. Kaltenbacher: Predicting spatial distributions of Lighthill's aeroacoustic source terms using steady-state RANS simulations in Turbocharger compressors. *Journal of Aerospace Engineering* 35, 1 (2022) 04021101. [https://doi.org/10.1061/\(ASCE\)AS.1943-5525.0001338](https://doi.org/10.1061/(ASCE)AS.1943-5525.0001338).
48. A. Hüppe: Spectral finite elements for acoustic field computation. Ph.D. Thesis. Alpen-Adria-Universität Klagenfurt, 2012.
49. Siemens Product Lifecycle Management Software Inc., STAR-CCM+. <https://www.plm.automation.siemens.com/global/en/products/simcenter/STAR-CCM.html>.
50. S. Schoder, P. Maurerlehner, A. Wurzinger, A. Hauser, S. Falk, S. Kniesburges, M. Döllinger, M. Kaltenbacher: Aeroacoustic sound source characterization of the human voice production-perturbed convective wave equation. *Applied Sciences* 11, 6 (2021) 2614. <https://doi.org/10.3390/app11062614>.
51. Vienna scientific cluster 3. <https://vsc.ac.at/home/>.

Cite this article as: Freidhager C. Schoder S. Maurerlehner P. Renz A. Becker S, et al. 2022. Applicability of two hybrid sound prediction methods for assessing in-duct sound absorbers of turbocharger compressors. *Acta Acustica*, 6, 37.